Title

Geometric and rheological asperities in an exposed fault zone

Journal

Journal of Geophysical Research, 114(B02301)

Authors

Sagy, Amir

Brodsky, Emily E.

Publication Date

2009-02-05

Peer reviewed

Geometric and rheological asperities in an exposed fault zone

Amir Sagy[1,2] and Emily E. Brodsky[1]

Received 18 March 2008; revised 22 September 2008; accepted 3 November 2008; published 5 February 2009.

[1] Earthquake dynamics are strongly affected by fault zone structure and fault surface geometry. Here we investigate the interplay of bulk deformation and surface topography using detailed structural analysis of a fault zone near Klamath Falls, Oregon, combined with LiDAR measurements of the fault surface. We find that the fault zone has a layered damage architecture. Slip primarily occurs inside a 1–20 mm wide band that contains principal slip surfaces with individual widths of ~100 μm. The slip band sits atop a cohesive layer which deforms by granular flow. Several fault strands with total slips of 0.5–150 m also have cohesive layers with thicknesses increasing monotonically with slip. The thickness added to the cohesive layer per unit slip decreases with increasing displacement indicating that slip progressively localizes. The main fault is a continuous surface with 10–40 m long quasi-elliptical geometrical asperities, i.e., bumps. The bumps reflect variations of the thickness of the granular cohesive layer and can be generated by a pinch-and-swell instability. As the granular layer is rheological distinct from its surroundings, the asperities are both geometrical and rheological inhomogenities. Modeling slip along wavy faults shows that slip on a surface with a realistic geometry requires internal yielding of the host rock. Our observations suggest that the internal deformation processes in the fault zone include ongoing fracture, slip along secondary faults, and particle rotation. Granular flow is an important part of faulting in this locale. Slip surfaces localize on the border of the granular cohesive layer. The ongoing slip smoothes the surfaces and thus the structural and geometrical evolution of the granular layer creates a preference for continued of slip on the same surface. There is a feedback cycle between slip on the surface and the generation of the granular layer that then deforms and controls the locus of future slip.

Citation: Sagy, A., and E. E. Brodsky (2009), Geometric and rheological asperities in an exposed fault zone, *J. Geophys. Res.*, *114*, B02301, doi:10.1029/2008JB005701.

1. Introduction

[2] Faults evolve through a complex series of physical and chemical processes acting over seconds to millions of years and on scales of microns to kilometers. Fault zones form with discrete slip surfaces in the fault core [*Sibson*, 1977; *Chester and Logan*, 1986; *Cowan et al.*, 2003]. At the same time, the surrounding rock is damaged and deformed [*Shipton and Cowie*, 2001; *Sibson*, 1986]. The combination of these processes controls slip (seismic and otherwise) and stress evolution in the fault zone.

[3] One of the major determinants of slip distribution in an earthquake is the presence of asperities [*Lay et al.*, 1982]. Although the word ''asperity'' originally meant a bump on an otherwise smooth surface, seismic studies have inferred asperities from slip distributions. As the seismic data simply define the distribution of slip during the earthquake, the studies raise a fundamental question about whether the origin of the heterogeneities is primarily geometrical or rheological. In this paper we attack the same question but focus on the scale of the slip in a moderate to large earthquake. This is a much finer scale than is accessible through seismic inversions.

[4] Faults have geometric irregularities in the direction of the slip over a large range of scales [*Okubo and Aki*, 1987; *Power et al.*, 1987; *Peacock*, 1991]. They display segmentation, branching, and corrugations which indicate an ongoing nucleation and merging of brittle fractures [*Stewart and Hancock*, 1991; *Jackson*, 1987; *Lee and Bruhn*, 1996]. Other corrugations such as mullions or boudins occur along large lithological contrasts. For example, *John* [1987] described low-angle normal faults in Southern California with wavy geometries along hundreds of meters to kilometers and showed that the amplitude and the wavelength of corrugations vary with the lithology of the footwall. At the outcrop scale, slip surfaces often have polished striations generated by abrasion. They can also be affected by adhesive wear, pressure solution, and growth fibers [*Petit*, 1987; *Means*, 1987].

[5] The above picture might suggest that fault geometry is dominated by stochastic processes, but some measurements indicate that fault roughness evolves with slip.

[1]Department of Earth and Planetary Sciences, University of California, Santa Cruz, California, USA.
[2]Geological Survey of Israel, Jerusalem, Israel.

0148-0227/09/2008JB005701$09.00

Spectral analysis of the roughness parallel to slip orientation presented by *Power and Tullis* [1991] can be interpreted as nonfractal [*Ben-Zion and Sammis*, 2003]. Using ground based LiDAR and a laboratory profilometer, *Sagy et al.* [2007a] demonstrated that slip surfaces of small-slip faults are rougher than those that slipped larger distances. Ongoing slip might also generate statistically scale-dependent roughness. Surfaces of small-slip faults are relatively rough at all measured scales, whereas those of moderate-slip faults are polished at small scales but contain quasi-elliptical asperities at scales of a few to several meters [*Sagy et al.*, 2007a].

[6] In this paper we address the mechanism that generates this complex surface geometry by combining detailed structural analysis of the fault structure with measurements of its surface geometry at a particularly exceptional locale: The Flowers Pit Fault. The fault has a large and continuous surface exposed over a ~0.5 km hillside. The very fresh surface was unearthed recently, and there are many exposures of cross sections perpendicular to the fault. Thus the fault presents a singular opportunity for measuring the relationship between fault surface geometry and fault zone structure. The fault zone exhibits a consistent damage structure, similar to the structure of other fault zones in different tectonic regimes [*Chester and Logan*, 1986; *Chester et al.*, 1993; *Billi et al.*, 2003; *Agosta and Aydin*, 2006; *Chambon et al.*, 2006a]. Thus it may provide an example of general faulting processes in the brittle crust.

[7] The geological setting of the Flowers Pit Fault will be described in section 2. In section 3 we will discuss the topography of the fault surface with a focus on the 20–40 m scale bumps and the scale dependence of the accompanying roughness. Section 4 will describe the fault zone architecture starting from the highly localized slip surface and proceeding into the footwall. This detailed geological work will illustrate that there are distinct layers that exhibit varying degrees and modes of deformation including granular flow and brittle fracture. The thickness of a key layer, termed Layer II, will be tied to the surface topography. Section 5 explores how the fault zone evolves with increasing slip through both direct observations of secondary faults in the Flower Pit complex and a modeling exercise. The combined results of section 5 show that the internal deformation processes are involved in the generation, evolution, and destruction of the asperities. In this fault zone, we will find that asperities are simultaneously geometric and rheological features. They are manifestations of damage evolution in the fault zone. There are feedback processes that generate internal damage due to slip on the fault and then control the distribution of future slip through heterogeneities in the damage structure.

2. Geological Setting

[8] The Flowers Pit Fault is a young normal fault located southwest of Klamath Falls, Oregon (Figures 1a–1b). The fault belongs to the Klamath Graben Fault system in the northwest province of the Basin and Range [*Personius et al.*, 2003]. Quaternary and Holocene activity was found on several nearby faults from the same system [*Bacon et al.*, 1999], and the area is seismically active, including a sequence of magnitude 6 earthquakes in 1993 [*Braunmiller et al.*, 1995]. However, the instrumental and historical data do not record an earthquake that is definitively on this particular fault. The fault itself is exposed by recent quarrying, and thus the surface is fresh (Figure 1c). The exposed footwall contains mostly andesite sequences. Fine-grained sandstone and arkose layers with thicknesses of a few meters appear above the wide, faulted andesite layers. These lake deposits are horizontally layered and covered by newer andesite and basaltic flows. The uppermost exposed sediments are gravels that are uncomformably bedded on the andesite and on the sandstone.

[9] The fault strikes to the WNW and creates a zigzag pattern (Figure 1b). The displacement along the fault is localized along a relatively continuous fault surface. The fault is exposed along 550 m and includes three large surface exposures with a composite area of ~6000 m^2. We infer that the total displacement is at least 100–200 m based on the appearance of patches of sediments and coarse gravels on the hanging wall vertically diverted to about 100 m below their original locations on top of the hill.

[10] The current quarrying exposed three separated sections. The northwestern one dips 55°/242° (dip/dip direction) on its northwestern edge and curves to 57°/234° on the southern end. This segment is exposed continuously along 150 m without any major splitting or branching. The longest exposed sections in the direction of the slip orientation are 30 m long. Branches and secondary fractures are rarely observed. The middle segment dips 66°/204°. It is exposed along a relatively small zone, but includes areas of up to 37 m of continual exposure parallel to the slip direction (Figure 2b). Ongoing quarrying in this section also provides very good exposure of the fault zone. The southeastern segment (Figures 1c–1d) dips 64°/214°. This section is more eroded, and therefore fewer chunks of fresh fault surface are exposed. However, because of the erosion, this section provides many opportunities to observe the structure of the fault zone under the surface. The southeastern segment is bifurcated on its northeastern side into two separate segments (Figures 1b–1c). One segment has a total displacement <50 m and strikes NNW (Figure 1b), while the other is covered by gravels but probably merges with the middle section.

[11] The slip on all the segments is oblique and the orientation of the last slip is measured using tool marks and striations. We also use the dense LiDAR measurements to follow the orientation of larger geometrical irregularities such as bumps and depressions (Figure 2 and Appendix A). We found that the orientation of small scale marks and larger undulations are similar. The slip trend on the segments is 246°–271°. The slip sense and dip direction can differ by as much as 38°, as occurs on the middle segment.

3. Fault Surface Geometry and Roughness

[12] The analysis of the LiDAR survey demonstrates that the fault surface in the Flowers Pit fault is curved (Figure 2). The most striking geometrical features on the surface are elongated quasi-elliptical structures (Figure 2). The appearance of such bumps on fault surfaces complicates slip along shear surfaces. Such geometrical asperities can influence the near-fault stress field [*Chester and Chester*, 2000], resistance to shear, and fault gouge generation [*Scholz*, 2002].

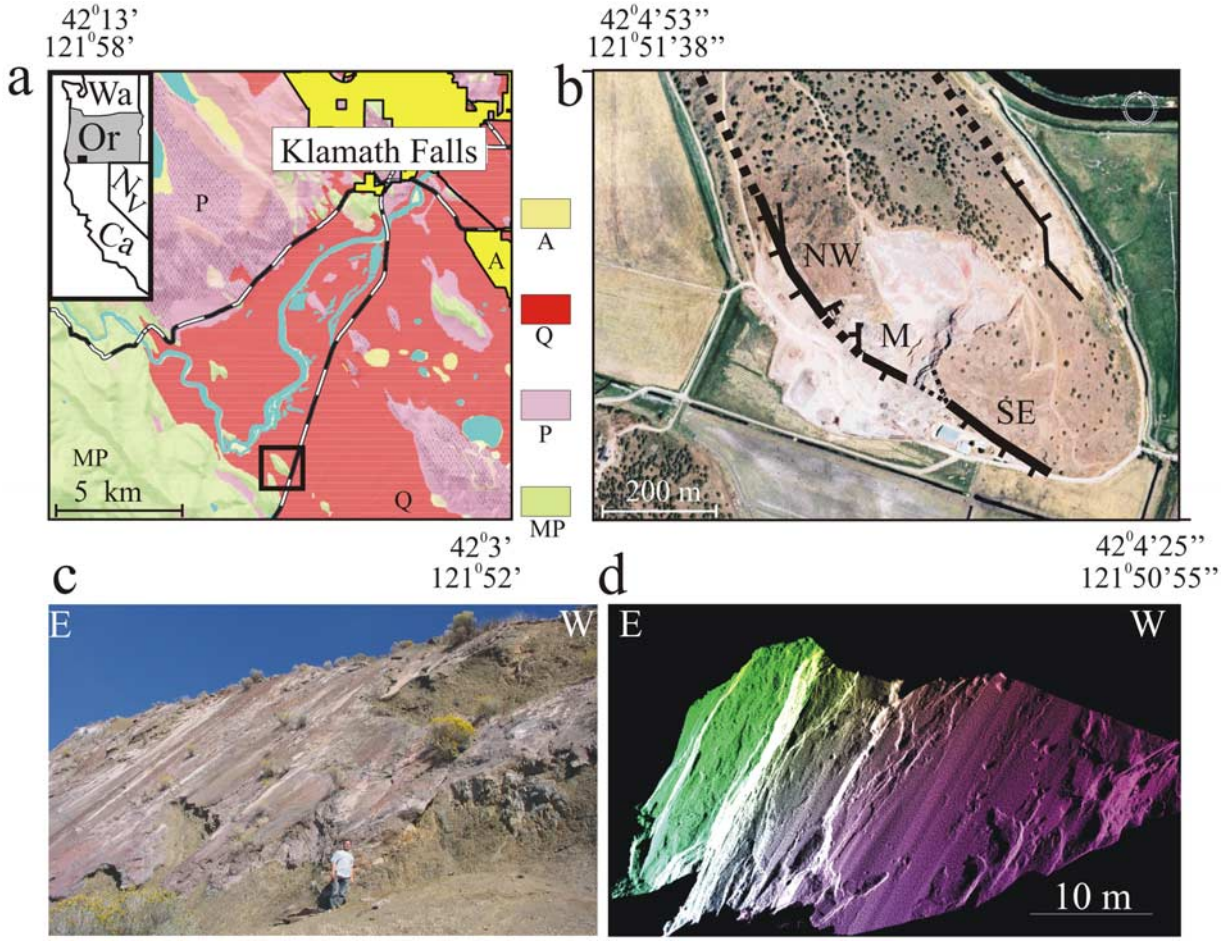

Figure 1. Geological map and pictures of the Flowers Pit fault. (a) Section of the geological map of Southwest Oregon showing the regional geological units [*Jenks*, 2007]. MP is Miocene to Pliocene basalt and andesite. Q is quaternary sedimentary rock. P is Pliocene volcanic flows. A is Alluvium and covered area. Inset in the upper left shows the regional location in the context of the western United States and the square on the geological map marks the Flowers Pit general locale. (b) The exposed (black lines) and the partly exposed (dashed lines) faults in Flowers Pit, marked on a Google Earth air photo. The Flowers Pit is located in the southwest part of a horst structure exposing normal faults that is striking northwest. Three large fault segments are marked by letters (SE: southeast segment, M: middle segment, NW: northwest segment). (c) Photo and (d) LiDAR image of the Southeast section of Flowers Pit Fault showing the continuous exposure of the surfaces. The image in Figure 1d is produced by scanning the surface with ~2 million measured points at a spacing of 0.5 cm.

Below we analyze the geometry of these structures. We will show that the characteristic geometry of these bumps is defined by its quasi-elliptical shape parallel to the surface (Figures 2b and 2f) and by the domination of large-amplitude curviness in its topography (Figures 2c and 2g).

[13] The typical bump shape is elongated with the major axis of the bump parallel to the slip orientation as recorded by small-scale striations and abrasional tool marks. Individual bumps cross multiple andesite layers. The exposed bumps are relatively long, and most are only partly preserved. Several examples on the Flowers Pit Fault demonstrate that the bumps are exposed as both protrusions and depressions (Figure 2). In general, the bumpy surfaces appear along the entire surface in the Flowers Pit Fault. Figure 2a suggests that at least in the northwestern fault segment their dimensions are relatively stationary, and they create a pattern on the surface with observed long axis of more than 20 m (in most cases the long axis is larger than the exposure) and short axis of 6 ± 2.5 m (measured as half of the wavelength perpendicular to the slip). Such quasi-elliptical structures are observed on other faults in the western United States [*Sagy et al.*, 2007a] and in Italy [*Sagy et al.*, 2007b] and might represent a common structure.

[14] The geometry of single bumps is presented in Figures 2b–2g. Here we present two separate examples of bumps from the northern and the middle segments of Flowers Pit Fault. Next to each image are profiles extracted from the LiDAR data parallel to the slip taken nearly along the long axis of the bump. The major axis of the bump in the northern part of the fault is larger than the exposure height, while the minor axis is 7 m long and the maximum

height relative to the closest depressions in its margins is 0.8 m. This bump is the best preserved of at least five large-scale bumps that have been identified on the northern part of the fault (Figure 2a). Partly exposed elongated protrusions and depressions are also presented in Figures 2e–2f. The largest bump (marked by I in Figure 2f) has a major axis length of more than 15 m, width of about 5 m and maximum amplitude of ~1m.

[15] The bumps are not simply a continuation of a self-similar roughness but actually are distinct features. In order to demonstrate this, we analyze the part of the topography explained by a single-wavelength at the location of the bumps and compare it to typical self-similar surfaces (Figure 3a). For the most pristine two bumps in the exposure (Figures 2b and 2f), the residual after fitting monochromatic signals are 2.7 and 3.9 mm, respectively. These residual RMS values are comparable to the noise level of the instrument (3 mm). To evaluate the significance of the observation, we generated synthetic self-similar surfaces with parameters picked to match the spectra at long wavelengths (Figures 3b and 3c). The synthetics have RMS $H = KL$ where L is a scale of measurement and $K = 0.5 \times 10^{-3}$. The RMS of the residuals after fitting with monochromatic signals is 12 ± 4 mm where the error bars are 1 standard deviation based on 500 random realizations of the self-similar surface. Using the self-affine relationship of $H = KL^{0.8}$ that is commonly used for fracture surfaces would further reinforce the discrepancy by increasing the signal at short wavelengths of the synthetic [*Bouchaud et al.*, 1993]. Thus, the observed bumps are resolvably different from the geometry expected for a self-affine surface.

4. Structure of the Fault Zone

[16] To investigate the interaction between the fault geometry and the evolution of the internal deformation (damage), we present a detailed analysis of the fault zone structure. We show that the fault zone is composed of distinct layers that are relatively continuous parallel to the fault surface, but abruptly change as a function of the distance from the surface (Figure 4). Although our damage classification is primarily based on large-scale structure and on the specific mechanical deformation, the layers are closely related to the more general classification of fault zone structure [e.g., *Sibson*, 1977; *Caine et al.*, 1996; *Woodcock and Mort*, 2008]. Layer I is a band of principal slip surfaces, Layer II contains cohesive granular material and is similar to structures called the cataclasite zone, and Layers III–V are fractured zones differentiated by fracture-mode and fracture intensity. The hanging wall is exposed

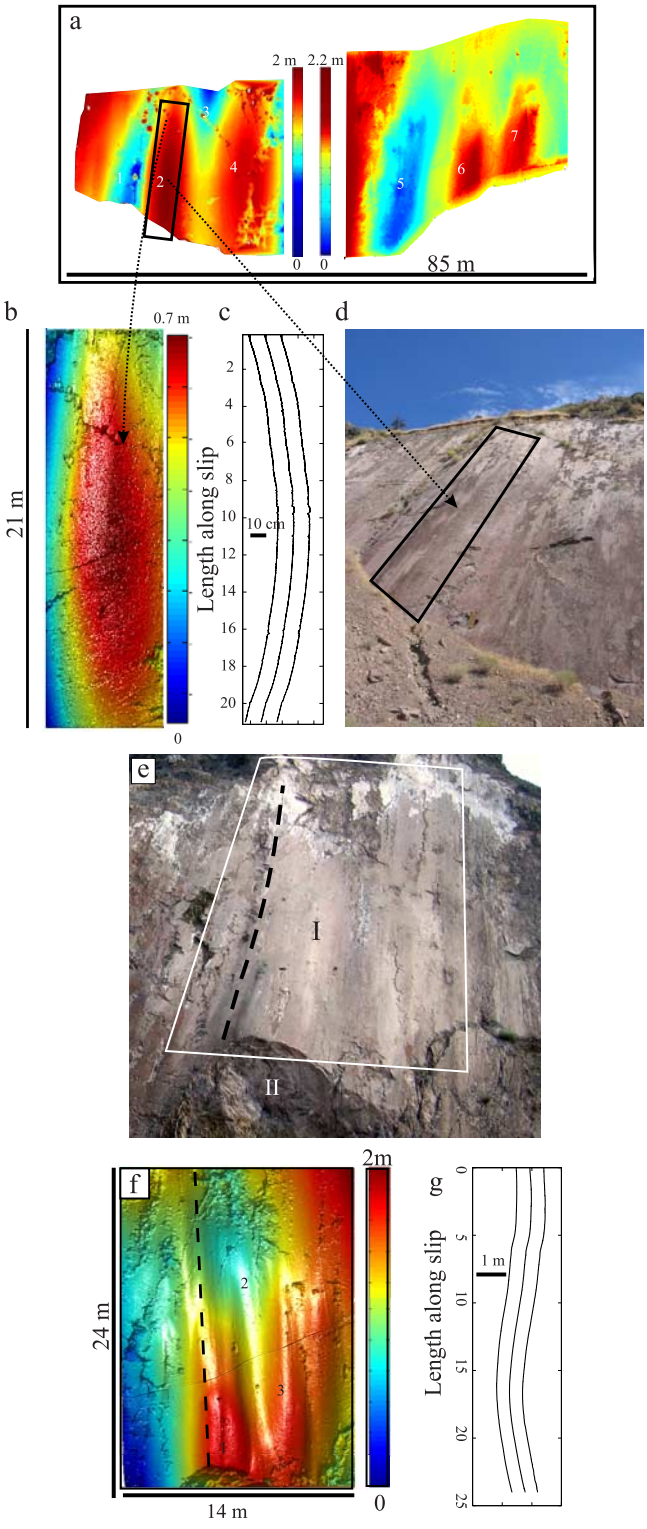

Figure 2. Fault surface in Flowers Pit. (a) Laser scan of the northern section of the fault. Patterns of quasi-elliptical bumps (numbered 1–7) in the surface observed above. The image is divided to two parts with separate elevation color-scale to improve the visibility the bumps. (b) Detailed data of a single well-preserved protruding bump (labeled "2" in Figure 2a). (c) Example profiles from the bump in Figure 2b that show the shape of the surface in the slip-parallel direction. (d) Photograph of the bump in Figure 2b. (e) Photograph of large bumps in the middle segment of the Flowers Pit fault. The main slip surface (Layer I) is underlain by a cohesive granular layer (Layer II). (f) LiDAR data of surface in Figure 2e. Bumps numbered 1–3. (g) Example profiles from bump in Figure 2e taken along the dashed line.

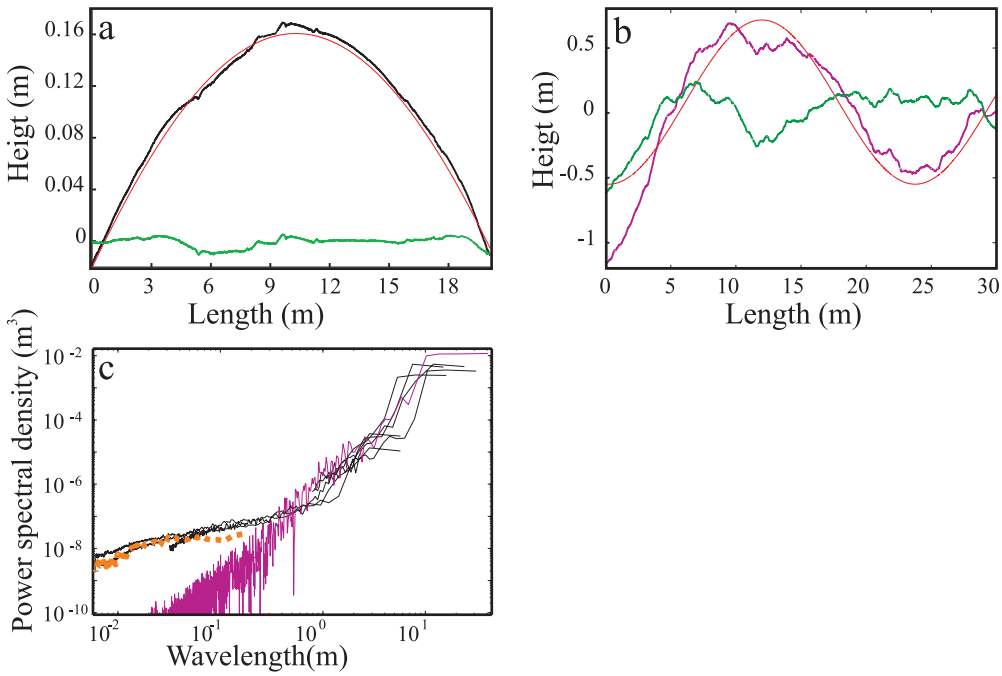

Figure 3. Topography and roughness of a bump parallel to the slip in Flowers Pit fault. (a) Black: Average of 176 topographic profiles parallel to the slip along the middle of the bump in Figure 2b. Red: Best fit sine function to the data. Green: Residual of fit. (b) Synthetic self-affine surface consistent with the observed power spectra at large wavelengths. Magenta: Synthetic topography, Red: Best fit sine function to the synthetic, Green: Residual of fit. (c) Comparison of the measured power spectral density and the synthetic one used to generate Figure 3b. Magenta: power spectra for self-similar synthetic surface consistent with the observed power spectra at large wavelengths ($H = K\lambda^{\zeta}$, $\zeta = 1$; $K = 0.5 \times 10^{-3}$). Orange: Noise level as determined from LiDAR scan of a flat board. Black: Power spectra of slip parallel profiles along the axis of bumps.

only in small patches and therefore it will not be discussed in detail.

4.1. Band of Principal Slip Surfaces (Layer I)

[17] Directly adjacent to the fault surface there is evidence for extreme localization on multiple slip surfaces accompanied by abrasional, fluid injection and granular flow structures. These structures are contained within a thin reddish layer (Figure 5a) that is usually 0.1–5 mm wide but occasionally reaches a width of 2 cm. The layer is exposed in very fresh zones on the fault. In more eroded areas, the layer partly fills elongated striations and indicates abrasive wear [*Petit*, 1987]. Examination of samples from this zone under a microscope reveals that the region typically contains one to three slip surfaces which are expressed by linear fine-grained bands inside altered granular material (Figures 5b–5d). The mineralogy of this layer contains 90% plagioclase. However, the reddish color in this layer (Figure 5a) is contributed by hematite as determined by X-ray diffraction (XRD).

[18] The slip surfaces are parallel to the primary surface and are distinguished from the surroundings by particle size. Typical slip surface thickness is 100–500 μm (Figure 5c). Using SEM analysis, we found that the sizes of the fragments inside a single slip band range between 10 μm and 0.1 μm (Figure 5b). The small particles are mostly shattered crystals and are much less rounded than the larger particles between the bands. As the size, shape and color of grains varies between the slip surfaces, we infer that several slip episodes are recorded.

[19] In many cases, we observed secondary fractures that branch from the slip surfaces (Figure 5c). Interestingly, we found that the granular injections penetrated only to one side of the fault (toward the footwall). The fractures tend to fork at high angle to the surface and then rotate to 50°–70° from the main slip surface. They are filled by the same fine-grained material as the main band. The observed branches extend no more than a few millimeters. The branches inject the fine-grained material into the layer below (Layer II), thus sometimes creating islands of fine-grained material (Figure 5c) in a sea of coarser-grained material. Similar secondary cracks are also observed at a larger scale (Figure 5a) where the fine-grained material of the principal slip zone is injected a few centimeters into the layer below.

[20] These branches are evidently opening-mode fractures because they do not shear the slip surfaces; they inject fine-grained material and contain secondary veins (Figure 5d). The veins are evidence of the existence of fluids during slip. The overall picture strongly suggests that the branches are hydrofractures which indicate internal pressurization of the slip surface [*Byerlee*, 1990; *Rice*, 1992; *Brodsky and Kanamori*, 2001]. The association with injected material suggests increased internal pressure. When the internal pressure exceeds the confining pressure by the tensile strength of the rock, a hydrofracture might be generated perpendicular to the main compressive stresses. In this case, the granular material has no tensile strength and the fault is near-surface, so only moderate pressures may be needed.

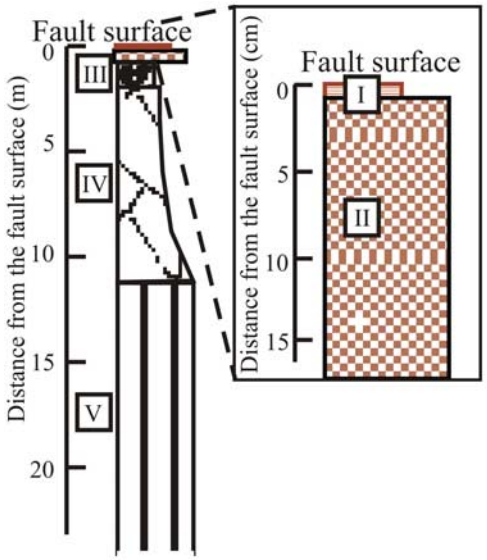

Figure 4. Damage characteristics of the Flowers Pit Fault from (top) the exposed surface toward (bottom) the footwall described by schematic stratigraphic column. The term "layer" is used here to describe the damage as the fault zone displays structure that is relatively continuous parallel to the fault surface but abruptly changes as function of the distance from the surface. The lengths of the boxes qualitatively indicate the rock cohesiveness. I: Band of slip surfaces (0.1–20 mm); II: Cohesive granular layer (0.05–1 m); III: Noncohesive fragmented layer (0.3–2 m); IV: Nonsystematic joints and fractures (~10 m); V: Jointed zone (>50 m).

Hydrodynamic lubrication with slurry of viscosity of 10 Pa s in the observed 100 μm wide bands with thickness variations of 0.1% will result in a pressure increase of 50 MPa due to the shearing of the fluid over 1 m of slip at a typical earthquake slip velocity of 1 m/s [*Brodsky and Kanamori*, 2001]. This overpressure is sufficient to drive the injections at depths up to nearly 2 km.

[21] Fluidization and ductile deformation are also documented in this band. A well- preserved section of Layer I was found above depressions or in relatively planar zones of the slip surface. In a few locations, the layer reached a thickness of ~2 cm. Figures 5e–5f shows a thin-section from this thick region. The upper part of the section (Figure 5e) shows planar subparallel slip bands that shear granular medium from Layer II. On the lower part (Figure 5f) however, wavy layering and boudinage structures appear in some of the layers, thus indicating ductile deformation of the layered medium and fluidization of the granular material. Foliated gouge structure (Figure 5e), and ductile and flow deformation of the gouge (Figure 5f) have been detected in experiments of shear of different rocks under dynamic friction conditions [*Boutareaud et al.*, 2008, *Mizoguchi*, 2004].

4.2. Cohesive Granular Layer (II)

[22] Layer II is the most distinctive layer in the fault zone. It contains cohesive rock that is persistent over the entire exposure. In the middle and the southern segments Layer II is 5–100 cm thick; however, in most of the exposure it is about 10–20 cm. As will be shown below, Layer II provides evidence for continuous internal deformation by granular flow, fracturing, and slip. "Granular flow" is a rheological term for relative rotation of solid particles during bulk deformation [*Campbell*, 1993]. This internal rotation of particles distinguishes granular flows from more commonly studied rheologies like elasticity or Newtonian viscosity [*Campbell*, 1993; *Mair and Hazzard*, 2007].

[23] The layer contains aggregates of crystals comprised mainly of plagioclase rotated inside a matrix of finer particles that includes single crystals or fragments of plagioclase (Figure 5c). The grains generally have dimensions of a few millimeters to a few centimeters. Extremely small-scale grains (diameters <1 μm) appear between the larger grains (Figure 5c) as observed on other faults [*Engelder*, 1974]. The roundness of some large grains in this layer (Figure 5c) suggests that significant particle rotation occurred during faulting.

[24] One of the mechanisms to bring small grains into Layer II is the injection of fine-grained material from Layer I (Figures 5a, 5c–5d). Such injections of fluids mixed with ultrafine grains contribute to cementation as evidenced by the vein in Figure 5d. Interestingly, we found no clear correlation between particle size and distance from the fault surface inside Layer II. In most cases, grains' radii in Layer II can achieve 1–3 cm only a few millimeters from the fault surface, which is the same order of magnitude as grains that are a few centimeters from the fault surface. Consequently, we infer that the cohesiveness of the layer is a result of the ongoing granular deformation, which increases the adhesive forces between comminuted grains as the surface area increases [*Gilbert et al.*, 1991], repacks the rock volume to a denser configuration [*Aydin*, 1978], and promotes fluid transport into the layer (Figure 5d). The combination of effects lithified the granular material. X-ray diffraction analysis of this region suggests no evidence of cementation beyond that represented by the injection features of Figure 5d.

[25] Brittle deformation at a larger scale is also observed in Layer II. Joints that cross the entire layer are likely connected to the extension of this zone during the ongoing faulting. Small normal faults with displacements of a few millimeters appear mostly at acute angles to the main fault surface. In most cases, these faults have a sense that is subparallel to the slip orientation recorded by the striations and they typically cross Layer II entirely, creating an S-shape in cross section. Continuous volumetric deformation of the layer is evidenced by small faults with spacing of a few centimeters that fragment the layer. Such faults indicate regranulation of the already cohesive layer.

[26] The surface undulations discussed in the fault geometry and roughness section are related to abrupt variations in the Layer II thickness. The layer widens under fault surface protrusions. For example, the maximum height of the bump in the right side of Figure 6a is 45 cm relative to the nearest depression on its right side. The maximum width of Layer II there is 110 cm. Under the depression on the left side, the minimum width of the layer is 5 cm. Figure 6b presents two more examples of the thickening of Layer II under the bumps and thinning of the layer under depressions. The maximum exposed thickness of Layer II in Figure 6b (top left) is 0.6 m, while the maximum amplitude compared to the nearest depression is 0.35 m. Under the nearest depression (Figure 6b, top right), the width of Layer II is again

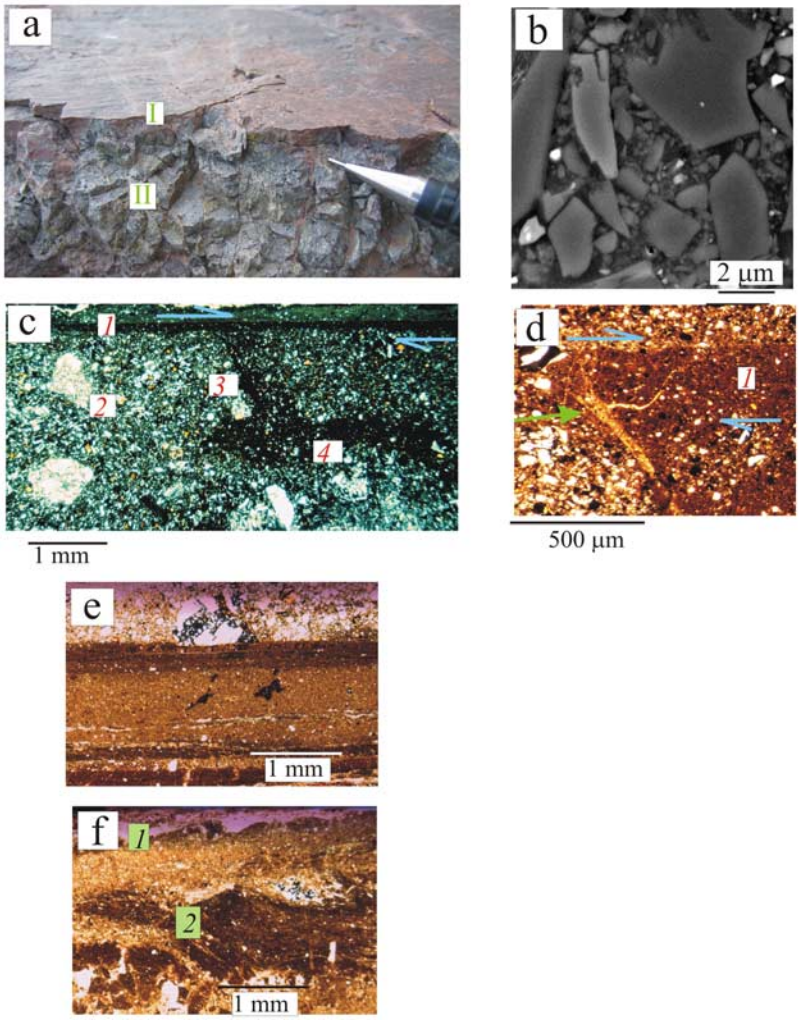

Figure 5. Photographs of field exposures and thin sections of the slip band zone (Layer I) and the upper part of the cohesive granular layer (Layer II). (a) A photo of the slip surface shows the extremely polished Layer I above the cohesive Layer II. The pen point is on fine material from Layer I that is injected to Layer II. The photo is rotated so that the fault surface is horizontal. (b) Scanning Electron Microscope (SEM) image of grains on slip zone in Layer I. (c) Layer I and II structure with key points labeled: (1) Typical sharp slip surface (100 microns wide). (2) Below the slip surface is Layer II which contains rounded aggregates of plagioclase and single crystals fragments. (3) Fracture that contains grains from the slip band and penetrates Layer II. (4) Zone of small-scale particles generated by the intrusion of Layer I grains. (d) Close-in view of evidence for opening modes involving fluid flow. Feature labeled 1 is the slip surface. The arrow indicates a vein inside the branching fracture. (e) Thick zone of Layer I showing several subparallel slip surfaces underlain by a fluidized ductile shear zone. (f) Fluidized deformation with wavy layers (labeled 1) and boudins (labeled 2). Figures 5e and 5f are continuous in the sample.

5–10 cm. In all six examples exposed, we found that Layer II thickens under the bumps (Figure 6c). Following this observation, we infer that the wavy appearance of the surface is due to variations of thickness of Layer II.

[27] Figure 7 provides evidence that bumps are deformed in a brittle manner and destroyed during slip as the geometry of the slip surface evolves. In contrast to the general correlation between bump appearance and the thickening of Layer II (Figure 6c), Figure 7a has a relatively thick Layer II with no clear bumpy appearance. Secondary normal faults that cross the layer at a sharp angle to the main surface appear in the photo. Figure 7b shows similar normal faults that are associated with extension of the layer parallel to the slip. The displacement on these faults separates the entire bumpy structure into rotated blocks crossed by the present main surface.

[28] The cartoons in Figure 7 present our interpretation of the observation. Following our previous observations in Figure 6, the relatively thick Layer II in Figure 7a suggests that once it was a bump, but with continuation of slip the bump was worn and truncated to generate the smooth current main slip surface. Such a domino-like collapse is typical for layer perpendicular compression of a competent layer inside a less competent medium when the competent layer becomes extremely stiff or the amplitude of the bumps becomes extremely large [*Johnson and Fletcher*, 1994; *Goscombe et*

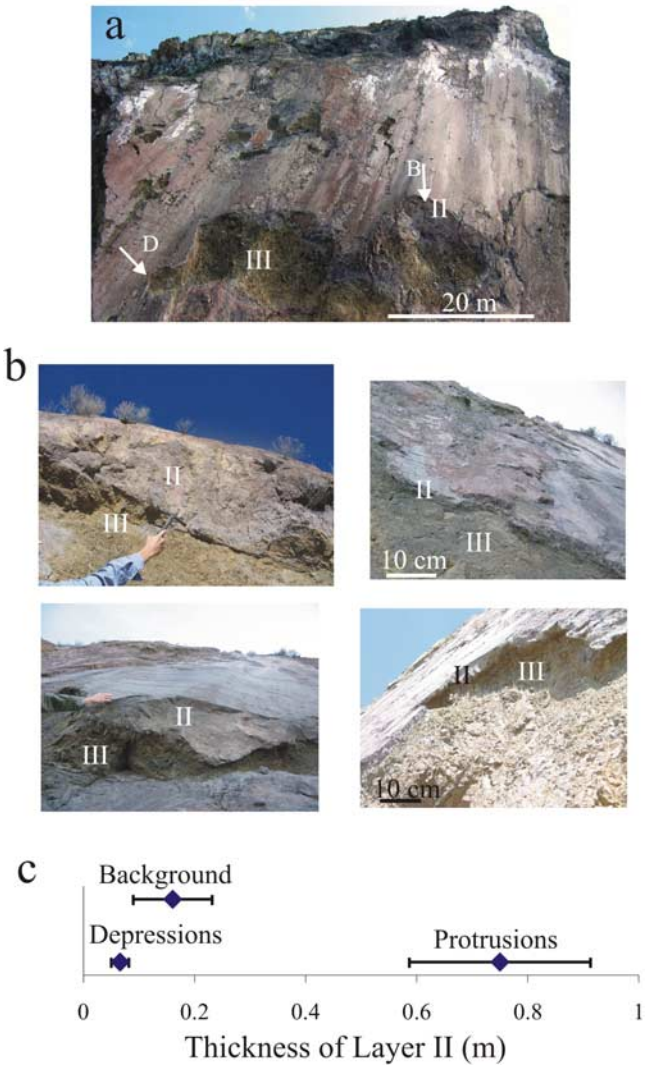

Figure 6. Variations of the width of Layer II under protrusions and depressions of the fault surface. (a) Variations of Layer II within the exposure of the middle part of Flowers Pit Fault surface. The biggest bump (marked by B) overlies the most thickened Layer II with a width > 1 m at the tip of the arrow. The largest depression (marked by D) overlies the most thinned Layer II with a minimum width of 5 cm. Smaller perturbations of the width of Layer II are also observed under smaller protrusions and depressions. (b) Two examples of local thickening of Layer II. Under protrusions (left) while thin appearance of the layer is observed under depressions (right). (c) Maximum observed width of Layer II under large bumps measured from six protrusions, and minimum width of Layer II measured under 10 large depressions. The background values measured in areas with relatively small amplitude variations of the surface (32 measurements). Error bars indicate 1 standard deviation.

al., 2004]. Thus, although Layer II is more cohesive than the surrounding damage zone (the hanging wall and Layer III), it still deforms with increasing slip and the current bumps shown in Figures 2 and 6 are probably transient features.

4.3. Noncohesive Fragmented Layer (III)

[29] Layer III has two main characteristics. First, it is much less cohesive and fragments easily. Second, deformation has destroyed the original mesostructures of the andesite (beds, veins, and fractures), but in contrast to the observations in Layer II, the microstructure is generally well-preserved (Figure 8).

[30] The layer is 0–2 m wide. The width variability is probably due to internal shear flow and stretching. We found no correlation between the Layer III and the topographical variations of the fault surface. Particle diameters are between a few millimeters and 30 cm. In some cases, several secondary faults from Layer II penetrate dozens of centimeters into Layer III and then die out (Figure 7). Under a bump, Layer III is always separated from Layer II by a fault (Figure 7). Elsewhere, the transition from cohesive to noncohesive material occurs over a few centimeters.

[31] Layer III is 90% plagioclase feldspar, like the host rock and Layer II. Structurally, however, the fragments differ from those in Layer II in that the particles are cut by opening-mode fractures and shear bands that are a few millimeters to a few centimeters apart (Figure 8). The shear bands contain high concentrations of small faults in conjugate geometry. The particles inside the shear bands include sheared plagioclase grains as small as <1 μm. There is no preferred orientation for the shear bands or for the tensile fractures (Figure 8). Outside of the shear bands, unfractured plagioclase crystals typically have 50–200 μm long axes and the original magmatic structures are usually preserved (Figure 8). The crystals are chemically altered along fractures and sometimes inside the fragments.

[32] Interestingly, remnants of the hanging wall have very similar structure and bulk deformation as Layer III. If such noncohesive material also borders Layer I and Layer II on the hanging wall side, it can explain the preservation of the bumpy topography of the cohesive zone as it likely deforms easily to accommodate the changes in geometry. In many places in the footwall, Layer III is separated from Layer II by a fault (Figure 7). The observations suggest that a symmetric sandwich could be developed with Layer II in the middle bordered by slip bands (Layer I) and Layer III on each side. Yet, in most of the observations of the Flowers Pit Fault only one slip surface is dominant while the other has been abandoned.

[33] The above observations of fracture and shear suggest that the noncohesive Layer III is a product of faulting. In addition, less competent flows in the andesite sequence might also contribute to the development of the noncohesive zone. Such noncohesive layers tend to stretch and flow along the fault. However, we found that far from the fault all of the exposed andesite flows have large fragments and are cohesive. Moreover, the noncohesive layer is not unique to Flowers Pit or to the specific lithology. Similar deformation zones were observed in other normal faults that occur in different tectonic and lithologic environments [*Chambon et al.*, 2006a].

[34] In summary, the observed microscopic and macroscopic deformation in Layer III includes fracturing and shear in its entire volume; however, the amount of rotation and comminution are small compared to Layer II. One way to explain these observations is by breakages due to mismatch of the fault surfaces during sliding [*Sibson*,

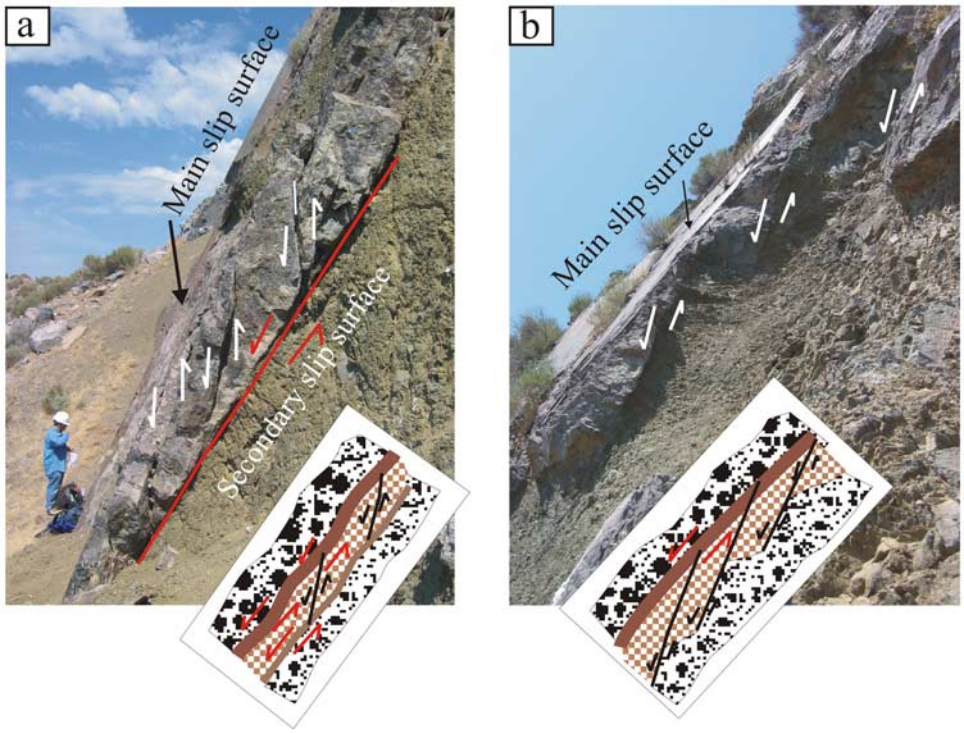

Figure 7. Thick exposure of Layer II below the main fault surface. A clear sharp difference between the cohesive appearance of Layer II and the noncohesive Layer III is observed. (a) Small normal faults with a few centimeters of slip (white arrows) appear in Layer II. A sharply localized secondary fault parallel to the main one is exposed between Layer II and Layer III. (b) Similar example which demonstrates the development of boudins in Layer II under sharp main slip surface. The interpretation in the text suggests that boudinage and decapitation of the bumps generates the observed structure.

1986], combined with smearing of noncompetent andesite flows parallel to the slip surface [*Aydin and Eyal*, 2002].

4.4. More Distant Deformation

[35] Beyond Layer III, we observe the original macroscopic features of the host rock such as flows and layers, although the rocks are still highly fragmented. Layer IV is a zone in which a dense net of small faults and joints appears with more coherent structure at the mesoscale. Intensity and fragmentation of fractures in Layer IV gradually changes and is influenced by the primary width and rheology of the host andesite layers.

[36] Layer V is defined as the zone which is dominated by joint sets which appears perpendicular to the andesite layers, although local highly fractured zones still exist. Exposure limitations prevent measurement further than ~50 m from the fault.

[37] Figure 9 presents the spacing of fractures in the footwall as a function of the distance from the fault. All distances were projected to be normal to the exposed fault surface. The data include measurements from Layer III–V. Most of the data was collected by mapping fractures using a gridded frame [*Sagy et al.*, 2003]. We also used photographs to map the fracture density. In Layer III, fracture spacing was measured using photographs and thin sections (see an example in Figure 8).

[38] The most striking observation in Figure 9 is the localization of damage near the fault and the nonlinear decay of the fracture density. The measurements in the first meter are sampling fracture density in Layer III and its local environment. The cumulative offset that repeatedly deforms this layer results in very dense fracture spacing. Changes in the fracture density further from the slip surface are relatively small. Beyond Layer III, the fracture density falls off as approximately the square root of distance. The slope of the fracture density curve suggests that up to at least ~50 m from the fault surface fracture density is still influenced by

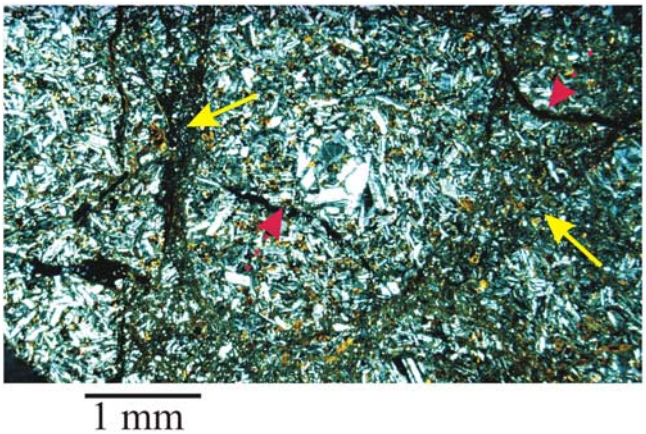

Figure 8. Thin-section from Layer III shows plagioclase rich andesite-hosted shear bands (yellow arrows) and fractures (red dotted arrows).

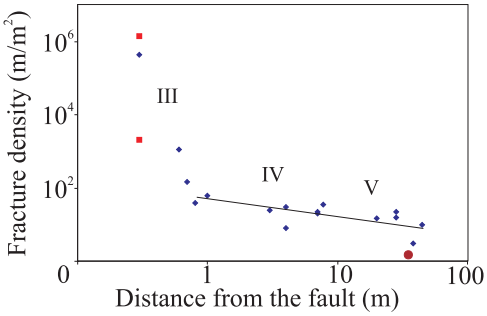

Figure 9. The density of fractures in the Flowers Pit Fault. Density is measured as total fracture length per area as a function of the distance from the fault. Blue diamonds show density values calculated by mapping fractures in an area with a gridded frame and photographs. Beyond Layer III fracture density decays roughly as the square root of distance (black line). The two red squares are values of fracture density measured in four thin sections (such as in Figure 7) from two different locations in Layer III. In these measurements, shear bands counted as fractures and their internal deformation is neglected. Brown circle represents the density of systematic large open cross-layer joints.

the fault. We did not manage to measure the background fracture density directly.

[39] About 10–30 m and further from the fault (Layer V), most of the observed fractures are opening-mode joints. Some of them are subparallel to the main fault segments. They cross layers, are open up to 1–5 cm when exposed, and can reach dozens of meters in height. They are probably related to the extension of the footwall near the fault [*Sagy et al.*, 2003]. However, the spacing of these joints is much smaller than the average fracture density which further reinforces the conclusion that the fault is still affecting the damage at the most distant measurements in Figure 9.

5. Structural Evolution of the Fault Damage and Fault Surface

5.1. Development of the Cohesive Layer With Slip

[40] The cohesive layer (Layer II) adjacent to the slip surface is not unique to the main fault. Similar layers also appear in branches of the main fault and in secondary faults in the fault zone. We showed that one of the principal characteristics of this layer is that grains are shaped by rotation and comminution (Figure 5). In this respect, the layer differs from the deformation zone further from the fault surface (Layers III–V) which is mostly fractured and fragmented. It is also different from the slip band zone (Layer I). Experiments suggest that such layering architecture is a typical outcome of deformation in granular material [*Mueth et al.*, 2000] and strongly dependent on the roughness [*Chambon et al.*, 2006b]. Following this observation we deduce that Layer II is closely related to wear material that is generated in shear experiments [*Kato and Adachi*, 2000].

[41] Figure 10 demonstrates the relationship between fault displacement and thickness of the cohesive layer (Layer II) in six individual faults in the Flowers Pit fault zone. The measured faults are the main fault, the fault that borders the horst from NE (Figure 1b), and four smaller faults. We measured the displacement of these faults using the layer offsets. Thickness of the cohesive layer was measured in 5–40 places along each fault, depending on the exposure. As the data was collected only in the Flowers Pit Fault zone, it represents similar rocks that deformed under similar physical and chemical conditions. We found that the cohesive Layer II is generated in an early stage of the fault and continues to evolve (Figure 10). However, on very small faults (displacement <0.5 m) Layer II could not be identified.

[42] The observations suggest a monotonic, nonlinear positive correlation between the displacement on the fault and the thickness of the cohesive granular layer. Figure 10 also suggests that the increasing thickness with increasing displacement (dT/dx) decreases as a function of the displacement (x), i.e., $d^2T/dx^2 < 0$. The saturation of the thickness results in a deviation from the linear trend discussed for faults elsewhere [*Scholz*, 2002].

[43] The nonlinear trend is consistent with the decrease of asperity amplitude during fault evolution that we measured in our previous study that compared the roughness of faults with differing slips [*Sagy et al.*, 2007a]. The decrease of the thickening with slip is comparable to the exponential decay of the wear production with increasing slip during the asperity-breaking stage (or running-in wear stage) of laboratory experiments [*Queener et al.*, 1965; *Wang and Scholz*, 1994; *Wong et al.*, 1998]. However, in these experiments the length of the slip surface is constant, but the dimension of a

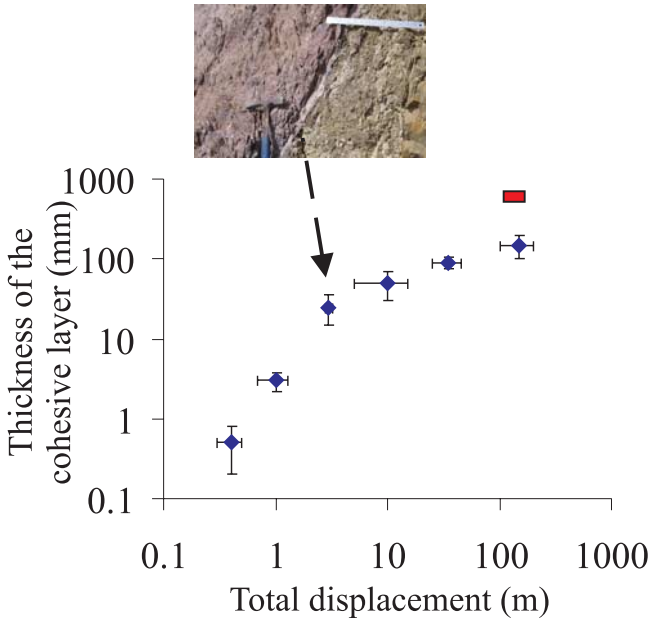

Figure 10. Thickness of the cohesive layer (Layer II) as a function of displacement for six different faults in the fault zone (including the main fault). In most of the exposures on the main fault the cohesive layer thickness is 10–20 cm. However, under protruding bumps the layer is always thickened and the width locally can exceed 1 m (red rectangle). The photo above shows the layer in a fault that is displaced 3 m.

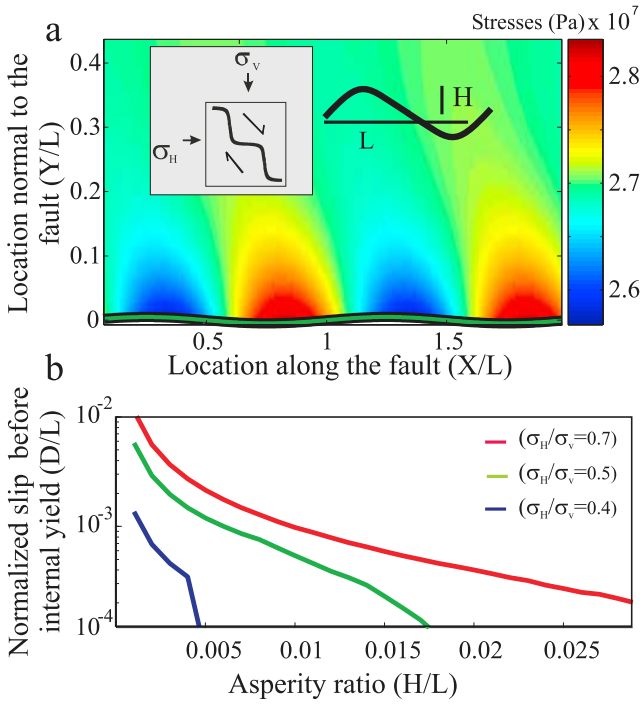

Figure 11. Modeled stress field due to slip on a wavy fault. (a) Calculated values of the maximum compressive principal stress σ_1 following the model of Appendix B with a realistic noncritical stress ratio $\sigma_H/\sigma_V = 0.5$, fault dip of 60°, σ_v equal to the lithostatic stress at 1 km depth, and slip $U = 0$ m. We used the topography measurements (Figures 2 and 3) to define a typical asperity aspect ratio, $H/L = 5 \times 10^{-3}$ (inset shows modeled fault geometry). (b) Critical slip distance for yielding on wavy slip surface as a function of asperity ratio, H/L, for three different stress ratios. A larger amount of slip before internal yielding is predicted for smoother surfaces.

natural fault is a function of the total offset on the fault [*Scholz*, 2002].

[44] Thus, the decrease of the layer production with slip is evidence of the localization and maturation processes during fault slip. Although variations in the layer thickness still exist as evidenced by the bumps (Figures 2 and 6), the slip on average is progressively localized as a function of the displacement.

5.2. Internal Failure During Slip on Wavy Faults With Bumps

[45] Let us now investigate the constraints on an earthquake that could occur on an active fault like the Flower Pit exposure. If the fault is loaded during the interseismic period and responds by slip along a preexisting surface during an earthquake, we can calculate the stresses around such a fault before the host rock yields. We will use this calculation to test how much a wavy fault can slip before breaking the host rock.

[46] We simplify the geometry and calculate the stresses near a 2-D wavy fault using a semianalytical approach [*Saucier et al.*, 1992; *Johnson and Fletcher*, 1994; *Chester and Chester*, 2000]. The fault is modeled as a frictional contact embedded in an elastic medium. The fault is composed of a planar surface with a sinusoidal perturbation of amplitude H and wavelength L (Figure 11 inset). This configuration is nearly identical to that of *Chester and Chester* [2000]. However, *Chester and Chester* [2000] used farfield stresses that result in critical failure conditions on the mean plane of the fault. Since we are interested in developing failure off the fault plane, we investigate a more general set of farfield conditions where we specify the ratio of horizontal to vertical stresses and resolve them on the fault plane at a specified dip (Appendix B).

[47] Even prior to slip, the perturbation of the fault geometry results in a perturbance of the stress field due to the frictional boundary condition (Figure 11a). As expected, the value of the maximum principal stress (σ_1) increases with respect to the vertical stress in the front of the bump and decreases in the lee of the bump. Also, the influence of the geometrical undulations on stress perturbation is limited. At a distance of more than 10% of the wavelength, the undulations are negligible (Figure 11a).

[48] Stresses become larger with increasing slip. When the stress in the rock exceeds the local Coulomb threshold (equation (B4)), the host rock yields. We calculate the slip required to initiate yielding (Figure 11b). Smooth surfaces are predicted to absorb larger amounts of slip before internal yielding. Slip along a fault surface with realistic geometry requires internal yielding of the host rock. For example, slip of about 1–10 m without damaging the host rock requires a nonrealistic amplitude-wavelength ratio of $1{:}10^6$. For the realistic geometry of Figure 11a, the host rock is predicted to yield in the center of the bump with a displacement of only 0.2% of the wavelength of the fault surface roughness.

[49] The model suggests that earthquakes involve deformation of the host rock. This deformation can be an important source for energy dissipation and a contributor to earthquake arrest.

5.3. Formation of the Bumps

[50] The smoothness of the fault surfaces parallel to the slip at <1 m scales (see Figure 2b and *Sagy et al.* [2007a]), together with the present observation of bumps at scales of tens of meters are consistent with the preferential removal of the small-scale asperities during slip. In this case the bumps might be remnants of previous large-scale roughness. However, the external and internal structure of Layer II suggests that additional mechanism probably contribute to the present geometry. We observe that the fault surface bumps are manifestations of lenses of cohesive granular material (Figure 6). In places where Layer II is thick, the slip surface heaves upwards and vice versa. Since the dominant characteristic of Layer II is the significant granular internal deformation (Figure 5), it is natural to look for a flow explanation for the thick lenses.

[51] Brittle and ductile shear in layered rocks with significant rheological differences between them typically involve boudinages and mullions [*Smith*, 1975, 1977; *Johnson and Fletcher*, 1994; *Goscombe et al.*, 2004]. Figure 5f presents such a ductile deformation in Layer I. Interestingly, *Smith* [1975] pointed out that mullions were a form of pinch-and-swell instability that required two interfaces between layers. That is precisely what we see in Figure 6. The warping of the slip topography reflects a deformation of the entire Layer II. The bumps are consistent

with being mullions or boudinages in the sense of *Smith* [1975].

[52] The difference between mullions and boudinages is that mullions form with layer-parallel compression in a layer than is less competent than its surroundings while boudinages form in layer perpendicular compression in layer that is more competent than its surroundings [*Smith*, 1975]. At present, Layer II is stiffer than the surroundings and the boudinaging in Figure 7 suggests that this was the case, at least during the last episodes of the deformation. However, the appropriate rheology of the granular flow at the fault conditions is extremely uncertain [*Brodsky and Kanamori*, 2001; *Lu et al.*, 2007]. For an ordinary coefficient of friction in optimally oriented Andersonian faults, fault parallel compression is larger than fault normal, which would suggest that the mullion-type instability was a better explanation. However, the there is evidence that some faults have fault-normal compression, which would be consistent with the boudinage model [*Zoback et al.*, 1987]. Layer II include evidence of both granular flow (Figure 5) and brittle fracturing (Figure 7) which might point on increasing of the cohesiveness of the layer through the deformation and transformation from mullions deformation style to boudinage. Clearly, more rheological work is needed to evaluate these possibilities.

[53] Both mullion and boudinage instabilities are strongly wavelength-dependent. The most unstable wavelength with the highest growth rate is expected to dominate the preserved flow. The ratio of the wavelength to layer thickness of the most unstable wavelength is a function of the rheology of both layers. Thus is the rheology of both Layer II and III remains consistent with slip, but the granular Layer II thickens, the wavelength of the bumps should increase as well. The relationship between bump length and the thickness of the granulated Layer II is an observable test of the boudinage/mullion hypothesis that we will pursue in future work on other faults.

[54] Much more work is needed to fully validate this model for bump formation. Bumps on fault zones of various slip should be measured and their wavelengths compared to the local thickness of the granulated layer. The fault zone layer deformation should also be systematically measured in the laboratory and the appropriate rheologies used to predict the unstable wavelengths. Such work is beyond the scope of this primarily observational paper. For now, we confine ourselves to suggesting a plausible model for the observations in Flowers Pit Fault along with the above tests for future work.

5.4. Localization of Slip

[55] One of the most robust results of the field study is that the principal slip surfaces are on the edges of the cohesive granular zone. Although there is some distributed deformation throughout the fault zone as illustrated by the granular flow textures (Figure 5c) and the secondary faults in Layer II (Figure 7), the principal slip surface is clearly distinguished (see section 4.1). For instance, only on this surface do we see clear abrasional striations, the reddish hematite coating and the micron-scale fragmented texture of Figure 5b.

[56] There are at least two mechanisms leading to the slip concentration at the granular flow boundary. First of all, an interface between dissimilar materials commonly results in localization due to the difference in compliances. An imposed stress field results in different strains in the two media and, if the difference is large enough, offset results [*Kelly and Tyson*, 1965]. Second, granular flows have particularly pronounced boundary localization. The phenomenon motivates the usual practice of introducing sand paper into experimental configurations in order to generate internal deformations [*Campbell*, 1993]. *Lu et al.* [2007] observed in shear experiments that sand flows tended to localize slip into a region that extended $\sim$2 grain diameters from the wall of the shear cell. *Campbell* [1993] explains the localization as a result of the inability of a relatively smooth wall to transmit angular momentum. Since the curvature of the wall is much less than that of individual grains, movement of the wall does not start grains spinning relative to each other. The lack of relative rotation results in the grains being locked together (jammed) and simply sliding past the wall. In other words, near the wall, the frictional sliding threshold for individual grains is reached more easily than the moment threshold for rotation. Far from the wall, the interlocking grains effectively transfer angular momentum and relative rotation occurs in preference to sliding.

[57] The implication for natural faults is that the ongoing smoothing of the main surface and the generation of the cohesive granular layer act together to continue localization and slip. As the granular layer develops from wear particles, the slip remains at the boundary. Progressively, the boundary itself becomes smoother, abrasion is reduced and the rate of the granular layer growth decreases.

5.5. Cycle of Internal Deformation and Slip Surface Generation

[58] It has been previously recognized that fault topography can affect internal deformation off-fault [*Kim et al.*, 2004]. We have shown in this study that internal deformation also affects fault topography to form a feedback cycle. Slip on the fault surface produces wear particles that form cohesive granulated layer (Layer II) adjacent to the slip surface. Continued slip injects new particles into the granular layer. The granular flow deforms and has regions of variable thickness. These variations of thickness are accommodated by internal deformation in the noncohesive Layer III. The ponding of the grains may be governed by flow instabilities, akin to boudinages. The slip surface localizes on the edge of the cohesive granular layer because of the contrasting rheologies and the granular flow behavior. Since the primary slip occurs at the boundary, the thickness variations of the granular layer generate fault topography. The fault topography then controls future slip events and hence future internal deformation.

[59] Individual fault bumps do not persist over the long-term history of the fault, as illustrated by the preserved remnants of truncated bumps and the calculations of the internal failure conditions in Figure 10. Instead, bumps are dissected as new fault surfaces form. It is likely that a mature, thickened Layer II eventually becomes too stiff to deform internally leading to brittle truncation. New bumps are also continually being generated by the internal deformation of the granular layer.

[60] This feedback cycle of deformation and localization is profoundly different from the traditional view of fault zones as simple frictional contacts [*Brace and Byerlee*, 1966; *Scholz*, 2002]. It suggests that a complete model of either energy dissipation or stress accumulation must account for both the internal and surface deformation. Many of these processes have been included as pieces of the energy budget and fault dynamics, but their intimate relationships have not been recognized. The grinding and granular flow feeds the granular flow that in turn controls slip localization.

6. Conclusions and Implications

[61] We showed here that slip surface geometry is strongly connected to the fault zone architecture. The Flowers Pit Fault has a continuous surface with elongated quasi-elliptical asperities (Figure 2). The geometry of the fault surface is correlated with variations in thickness of the granular cohesive layer (Layer II). A protrusion of the surface indicates a thickening of the layer below it (Figure 6). As the granular layer is a separate rheological unit from its surroundings, the asperities simultaneously serve as both geometrical and rheological inhomogenities. Asperity generation is driven by the variation of rigidity during the evolving Layer II and Layer III. Abrasive wear on the surface (Layer I) and bulk granular flow in Layer II are acting together to generate a surface which is smooth at small scales but bumpy at scales greater than a few meters.

[62] The modeling of wavy faults demonstrates that the evolution of the fault in general and the cohesive layer in particular, involves deformation far from the slip surface. The modeling is supported by the field observations (section 4) that indicate three main deformation mechanisms in the fault zone: rotation of grains, fracturing, and slip. Thus, granular flow with considerable rotation of particles is a major mechanism for creating the observed structure of the fault zone (Figures 4 and 7). It is important to note that the host rock itself is not granular in origin and therefore granulation by fracturing and comminution occur during the faulting.

[63] The slip along small faults and the rotation of grains can be significant contributors to the dissipation of energy during slip events, in addition to heat generation by slip along the main surface and surface energy utilized in fracturing [*Wilson et al.*, 2005]. However, our observations (Figure 10) also suggest that the rate of wear production decreases as a function of slip. These observations together with the roughness measurements (Figure 3) indicate that less energy will dissipate in the fault zone as the fault matures. Thus, for a given amount of stress, slip along a mature fault is likely to be larger than slip on a relatively less mature fault.

[64] Even though deformation occurs in the bulk, the major slip surface of the fault tends to localized in 100 micron bands embedded in 1–20 mm wide zone on one or both sides of the cohesive layer. The main fault is confined on the borders of the layer although both sides of the layer (the hanging wall and layer III) are weaker (see also *Chambon et al.* [2006a]). Such localization of deformation is well documented in complex materials as the two dissimilar materials have different compliance and thus different strains as a result of the imposed stresses. The implication of this observation for natural faults is that the ongoing smoothing of the main surfaces and the generation of the granular cohesive layer act together to continue localization and slip.

[65] Therefore we suggest that fault structure and geometry both evolve with increasing slip. A cycle of damage and internal deformation ties the fault surface and layered architecture together. Together, the geometry and structure conspire to localize the fault. Together, they result in the continuation of slip within an extremely narrow zone.

Appendix A: Topography Measurements

[66] For measuring the geometry and the roughness of the fault surface over scales of 3 mm to 500 m, we use the Leica HDS3000 ground-based Light Detection and Ranging (LiDAR) tool. The scanner can aim its laser beam in a wide range and produce high-density measurements. The LiDAR has several advantages for our research compared to any other method. The accuracy of the measurements enables a reliable quantification of the data. The scanner also enables measuring of structures that are technically hard to approach, such as the middle segment of the Flowers Pit Fault (Figure 2a). Data that are collected from different locations are integrated to create a 3-D picture of large areas. The main advantage of the instrument for roughness measurements is, however, the number of the points sampled. A typical point cloud from a single scan can includes millions of points which can be interpolated to generate a topographic map or thousands of profiles (Figures 1 and 2). Thus, the technique allows a statistical approach when calculating roughness. The Flowers Pit Fault was scanned during two separate expeditions. The first focused on scanning discrete parts of the fault surface from different orientation and at different resolutions, from 3 mm to 2 cm, while the second was dedicated to continuous measurement of the fault surface at a resolution of 1 cm (Figure 1d). High-resolution measurements with point spacing of 3 mm were scanned from 20 to 40 m. All scanning expeditions included measuring a reference board which included small cubes with known heights of 3 mm, 6 mm, and 11 mm. We typically record range error of $\sim$3 mm in the line-of-sight direction, with the exact value varying with weather conditions. We use this reference to compare between the separate measurements and to define the accuracy of the measurement after the analysis. Measurements were then combined to create a complete picture of the fault geometry.

[67] For measuring roughness we sample the surface sections that are best preserved. However, it is almost impossible to find large zones in a natural fault that not partly harmed by erosion or by joints and small faults that cross the surface (see Figure 2). The scan data are rotated so that the mean surface is parallel to a major axis and the mean striation direction is vertical or horizontal. The striation direction is established by finding the orientation that maximizes the cross correlation between adjacent profiles [*Sagy et al.*, 2007a]. On each profile, spurious points with excessively large curvature (>4 standard deviations from the mean) were removed and data were interpolated across the gap. For example, we removed the sharp localized topography that generated by joints that cross the surface. For the

spectral analysis, the data fraction removed been limited to <3% in all cases, so the process does not affect the results.

[68] The power spectral density is a convenient measure of roughness as a function of wavelength as it is directly related to the RMS roughness [*Brown and Scholz*, 1985]. We calculate power spectral densities using a multitaper Fourier Transform method on each profile individually and averaging 200–600 spectra per curve. Each profile is individually detrended before computing the spectra. The elements p_i of the power spectral density (PSD) vector of the individual discrete vectors y as computed by the matlab function pmtm are

$$p_i = \frac{\frac{1}{N}\hat{y}_i^2}{1/\Delta x} = \frac{1}{N}\hat{y}_i^2 \Delta x \tag{A1}$$

where N is the number of points, $\hat{y}_i$ are the components of the Fourier transform and Δx is the sample spacing. The units of equation (A1) are m^3. As noted by other authors, different conventions for power spectral density exist in the literature [*Press et al.*, 2007, section 13.4].

Appendix B: Elastic Perturbation Model

[69] For calculating stresses along a wavy fault we follow equations (7a)–(7c) of *Chester and Chester* [2000] with a modification to the farfield condition. In their model, Chester and Chester performed a linear perturbation analysis of the stresses along a frictional discontinuity in an elastic homogeneous medium. Stresses are computed by adding the stresses that are contributed from small sinusoidal perturbations of a frictional surface to those which are generated by the planar surface. The governing equations for the stress on a fault surface parallel to the x axis that is perturbed around the $z = 0$ plane are

$$\sigma_{xx} = \bar{\sigma}_{xx} + Ale^{-lz}\{\frac{UEl}{4(1-\nu^2)}(-1+lz)\cos(lx) + \left[\bar{\sigma}_{zz}\left(1-k+2\mu^2\right) - \frac{\mu UEl}{4(1-\nu^2)}\right](-2+lz)\sin(lx)\} \tag{B1}$$

$$\sigma_{zz} = \bar{\sigma}_{zz} + Ale^{-lz}\{\frac{UEl}{4(1-\nu^2)}(-1-lz)\cos(lx) + \left[\bar{\sigma}_{zz}\left(1-k+2\mu^2\right) - \frac{\mu UEl}{4(1-\nu^2)}\right](-lz)\sin(lx)\} \tag{B2}$$

$$\sigma_{xz} = \bar{\sigma}_{xz} + Ale^{-lz}\{\frac{UEl}{4(1-\nu^2)}(-lz)\sin(lx) + \left[\bar{\sigma}_{zz}\left(1-k+2\mu^2\right) - \frac{\mu UEl}{4(1-\nu^2)}\right](-1+lz)\cos(lx)\} \tag{B3}$$

where $\bar{\sigma}_{ij}$ are the farfield stresses; A and l are the amplitude and the wavelength of the perturbations; E, ν, and μ are Young Modulus, Poisson ratio, and the friction coefficient, respectively; k is the farfield stress ratio $\bar{\sigma}_{xx}/\bar{\sigma}_{zz}$; and U is the displacement along the fault. We explore a range of farfield stresses defined by the ratio of the horizontal to vertical stresses and the dip of the fault plane.

[70] The host rock yields following a Coulomb failure criterion (Figure 11b). Failure occurs when the local difference between the principal stresses exceeds the internal frictional stress. This criterion is

$$\sigma_1 > \sigma_2 + 2\mu\sigma_2\left[\left(1+\mu^2\right)^{1/2} + \mu\right] \tag{B4}$$

where σ_1 and σ_2 are the maximum and minimum principal stresses, respectively [*Jaeger et al.*, 2007, equation (3.31)]. The stresses are calculated by solving equations (B1)–(B3) as a function of space and the given fault displacement U with prescribed farfield stresses. All calculation assume μ = 0.7.

[71] **Acknowledgments.** We thank Gary Axen, Andrea Billi, Judi Chester, Mai-Linh Doan, Jay Fineberg, Jeremy Hourigan, Margie Jenks, Thorne Lay, Ryan McKenzie, Max Taylor, and Nicholas van der Elst for their help on this work. A special thank is due to Bob Flowers who graciously allowed access to his quarry. This work was supported by the National Science Foundation grant EAR-0711575 and the Southern California Earthquake Center (SCEC).

References

Agosta, F., and A. Aydin (2006), Architecture and deformation mechanism of a basin-bounding normal fault in Mesozoic platform carbonates, Central Italy, *J. Struct. Geol.*, *28*, 1445–1467, doi:10.1016/j.jsg.2006.04.006.

Aydin, A. (1978), Small faults formed as deformation bands in sandstone, *Pure Appl. Geophys.*, *116*, 913–930, doi:10.1007/BF00876546.

Aydin, A., and Y. Eyal (2002), Anatomy of a normal fault with shale smear: Implications for fault seal, *AAPG Bull.*, *86*, 1367–1381.

Bacon, C. R., M. A. Lanphere, and D. E. Champion (1999), Late Quaternary slip rate and seismic hazards of the West Klamath Lake fault zone near Crater Lake, Oregon Cascades, *Geology*, *27*, 43–46, doi:10.1130/0091-7613(1999)027<0043:LQSRAS>2.3.CO;2.

Ben-Zion, Y., and C. G. Sammis (2003), Characterization of fault zones, *Pure Appl. Geophys.*, *160*, 677–715, doi:10.1007/PL00012554.

Billi, A., F. Salvini, and F. Storti (2003), The damage zone-fault core transition in carbonate rocks: Implications for fault growth, structure and permeability, *J. Struct. Geol.*, *25*, 1779–1794, doi:10.1016/S0191-8141(03)00037-3.

Bouchaud, E., et al. (1993), Statistics of branched fracture surfaces, *Phys. Rev. B*, *48*(5), 2917–2928, doi:10.1103/PhysRevB.48.2917.

Boutareaud, S., D. Calugaru, R. Han, O. Fabbri, K. Mizoguchi, A. Tsutsumi, and T. Shimamoto (2008), Clay-clast aggregates: A new textural evidence for seismic fault sliding?, *Geophys. Res. Lett.*, *35*, L05302, doi:10.1029/2007GL032554.

Brace, W. F., and J. D. Byerlee (1966), Stick-slip as a mechanism for earthquakes, *Science*, *153*, 990–992, doi:10.1126/science.153.3739.990.

Braunmiller, J., J. Nábelek, B. Leitner, and A. Qamar (1995), The 1993 Klamath Falls, Oregon, earthquake sequence: Source mechanisms from regional data, *Geophys. Res. Lett.*, *22*, 105–108, doi:10.1029/94GL02844.

Brodsky, E. E., and H. Kanamori (2001), The elastohydrodynamic lubrication of faults, *J. Geophys. Res.*, *106*, 16,357–16,374, doi:10.1029/2001JB000430.

Brown, S. R., and C. H. Scholz (1985), Broad bandwidth study of the topography of natural rock surfaces, *J. Geophys. Res.*, *90*(B14), 12,575–12,582, doi:10.1029/JB090iB14p12575.

Byerlee, J. (1990), Friction, overpressure and fault normal compression, *Geophys. Res. Lett.*, *17*, 2109–2112, doi:10.1029/GL017i012p02109.

Caine, J. S., J. P. Evans, and C. B. Forster (1996), Fault zone architecture and permeability structure, *Geology*, *24*(11), 1025–1028, doi:10.1130/0091-7613(1996)024<1025:FZAAPS>2.3.CO;2.

Campbell, C. S. (1993), Boundary interactions for two-dimensional granular flows. Part 2. Roughened boundaries, *J. Fluid Mech.*, *247*, 137–156, doi:10.1017/S0022112093000412.

Chambon, G., J. Schmittbuhl, A. Corfdir, N. Orellana, M. Diraison, and Y. Géraud (2006a), The thickness of faults: From laboratory experiments to field scale observations, *Tectonophysics*, *426*, 77–94, doi:10.1016/j.tecto.2006.02.014.

Chambon, G., J. Schmittbuhl, and A. Corfdir (2006b), Frictional response of a thick gouge sample: 1. Mechanical measurements and microstructures, *J. Geophys. Res.*, *111*, B09308, doi:10.1029/2003JB002731.

Chester, F. M., and J. S. Chester (2000), Stress and deformation along wavy frictional faults, *J. Geophys. Res.*, *105*(B10), 23,421–23,430, doi:10.1029/2000JB900241.

Chester, F. M., and J. M. Logan (1986), Implications for mechanical-properties of brittle faults from observations of the Punchbowl fault zone, California, *Pure Appl. Geophys.*, *124*, 79–106, doi:10.1007/BF00875720.

Chester, F. M., J. P. Evans, and R. L. Biegel (1993), Internal structure and weakening mechanisms of the San-Andreas Fault, *J. Geophys. Res.*, *98*, 771–786, doi:10.1029/92JB01866.

Cowan, D. S., T. T. Cladouhos, and J. K. Morgan (2003), Structural geology and kinematic history of rocks formed along low-angle normal faults, Death Valley, California, *Geol. Soc. Am. Bull.*, *115*, 1230–1248, doi:10.1130/B25245.1.

Engelder, J. T. (1974), Cataclasis and generation of fault gouge, *Geol. Soc. Am. Bull.*, *85*, 1515–1522, doi:10.1130/0016-7606(1974)85<1515:CATGOF>2.0.CO;2.

Gilbert, J. S., S. J. Lane, R. S. J. Sparks, and T. Koyaguchi (1991), Charge measurements on particle fallout from a volcanic plume, *Nature*, *349*, 598–600, doi:10.1038/349598a0.

Goscombe, B. D., C. W. Passchier, and M. Hand (2004), Boudinage classification: End-member boudin types and modified boudin structures, *J. Struct. Geol.*, *26*, 739–763, doi:10.1016/j.jsg.2003.08.015.

Jackson, P. (1987), The corrugation and bifurcation of fault surfaces by cross-slip, *J. Struct. Geol.*, *9*, 247–250, doi:10.1016/0191-8141(87)90030-7.

Jaeger, J. C., N. G. W. Cook, and R. W. Zimmerman (2007), *Fundamentals of Rock Mechanics*, 488 pp., Blackwell, Malden, Mass.

Jenks, M. (2007), Geologic compilation map of part of the Upper Klamath Basin, Klamath County, Oregon, *Open File Rep. O-07–05*, Oreg. Dept. of Geol. and Mineral Ind., Portland.

John, B. E. (1987), Geometry and evolution of a mid-crustal extensional fault system: Chemehuevi Mountains, southeastern California, in *Continental Extensional Tectonics*, edited by M. P. Coward, J. F. Dewey, and P. L. Hancock, *Geol. Soc. Spec. Publ.*, *28*, 313–336.

Johnson, A. M., and R. C. Fletcher (1994), *Folding of Viscous Layers: Mechanical Analysis and Interpretation of Structures in Deformed Rock*, Columbia Univ. Press, New York.

Kato, K., and K. Adachi (2000), Wear mechanisms, in *Modern Tribology Handbook*, edited by B. Bhushan, pp. 273–300, CRC Press, Boca Raton, Fla.

Kelly, A., and W. R. Tyson (1965), Tensile properties of fiber-reinforced metals: Copper/Tungsten and Copper/Molybdenum, *J. Mech. Phys. Solids*, *13*, 329–350.

Kim, Y. S., D. C. P. Peacock, and D. J. Sanderson (2004), Fault damage zones, *J. Struct. Geol.*, *26*, 503–517, doi:10.1016/j.jsg.2003.08.002.

Lay, T., H. Kanamori, and L. Ruff (1982), The asperity model and the nature of large subduction zone earthquakes, *Earthquake Prediction Res.*, *1*, 3–71.

Lee, J. J., and R. L. Bruhn (1996), Structural anisotropy of normal fault surfaces, *J. Struct. Geol.*, *18*, 1043–1059, doi:10.1016/0191-8141(96)00022-3.

Lu, K., E. E. Brodsky, and H. P. Kavehpour (2007), Shear-weakening of the transitional regime for granular flow, *J. Fluid Mech.*, *587*, 347–372, doi:10.1017/S0022112007007331.

Mair, K., and J. F. Hazzard (2007), Nature of stress accommodation in sheared granular material: Insights from 3D numerical modeling, *Earth Planet. Sci. Lett.*, *259*, 469–485, doi:10.1016/j.epsl.2007.05.006.

Means, W. D. (1987), A newly recognized type of slickenside striation, *J. Struct. Geol.*, *9*, 585–590, doi:10.1016/0191-8141(87)90143-X.

Mizoguchi, K. (2004), High-velocity frictional behaviour of Nojima fault gouge and its implications for seismogenic fault motion, 80 pp., Univ. of Kyoto, Japan.

Mueth, D. M., G. F. Debregeas, G. S. Karczmar, P. J. Eng, S. R. Nagel, and H. M. Jaeger (2000), Signatures of granular microstructure in dense shear flows, *Nature*, *406*, 385–389, doi:10.1038/35019032.

Okubo, P. G., and K. Aki (1987), Fractal geometry in the San Andreas fault system, *J. Geophys. Res.*, *92*(B1), 345–355, doi:10.1029/JB092iB01p00345.

Peacock, D. C. P. (1991), Displacements and segment linkage in strike-slip-fault zones, *J. Struct. Geol.*, *13*, 1025–1035, doi:10.1016/0191-8141(91)90054-M.

Personius, S. F., R. L. Dart, L. A. Bradley, and K. M. Haller (2003), Map and data for Quaternary faults and folds in Oregon, *U.S. Geol. Surv. Open File Rep.*, *03–095*, 550 pp.

Petit, J. P. (1987), Criteria for the sense of movement on fault surfaces in brittle rocks, *J. Struct. Geol.*, *9*, 597–608, doi:10.1016/0191-8141(87)90145-3.

Power, W. L., and T. E. Tullis (1991), Euclidean and fractal models for the description of rock surface-roughness, *J. Geophys. Res.*, *96*(B1), 415–424, doi:10.1029/90JB02107.

Power, W. L., T. E. Tullis, S. R. Brown, G. N. Boitnott, and C. H. Scholz (1987), Roughness of natural fault surfaces, *Geophys. Res. Lett.*, *14*, 29–32, doi:10.1029/GL014i001p00029.

Press, W. H., S. A. Teukolsky, W. T. Vetterling, and B. P. Flannery (2007), *Numerical Recipes: The Art of Scientific Computing*, 3rd ed., Cambridge Univ. Press, New York.

Queener, C. A., T. C. Smith, and W. L. Mitchell (1965), Transient wear of machine parts, *Wear*, *8*, 391–400, doi:10.1016/0043-1648(65)90170-5.

Rice, J. R. (1992), Fault stress states, pore pressure distribution, and the weakness of the San Andreas fault, in *Fault Mechanics and Transport Properties of Rocks*, edited by B. Evans and T.-F. Wong, pp. 475–503, Academic, San Diego, Calif.

Sagy, A., Z. Reches, and A. Agnon (2003), Hierarchic three-dimensional structure and slip partitioning in the western Dead Sea pull-apart, *Tectonics*, *22*(1), 1004, doi:10.1029/2001TC001323.

Sagy, A., E. E. Brodsky, and G. J. Axen (2007a), Evolution of fault-surface roughness with slip, *Geology*, *35*, 283–286, doi:10.1130/G23235A.1.

Sagy, A., E. E. Brodsky, N. van der Elst, F. Agosta, G. Di Toro, and C. Collettini (2007b), Geometrical and structural asperities on fault surfaces, *Eos Trans. AGU*, *88*(52), Fall Meet. Suppl., Abstract T44B–03.

Saucier, F. J., E. D. Humphreys, and R. J. Weldon (1992), Stress near geometrically complex strike-slip faults: Application to the San Andreas fault near Cajon Pass, southern California, *J. Geophys. Res.*, *97*(B4), 5081–5094, doi:10.1029/91JB02644.

Scholz, C. H. (2002), *The Mechanics of Earthquakes and Faulting*, 2nd ed., 471 pp., Cambridge Univ. Press, Cambridge, U. K.

Shipton, Z. K., and P. A. Cowie (2001), Damage zone and slip-surface evolution over (m to km scales in high-porosity Navajo sandstone, Utah, *J. Struct. Geol.*, *23*, 1825–1844, doi:10.1016/S0191-8141(01)00035-9.

Sibson, R. H. (1977), Fault rocks and fault mechanisms, *J. Geol. Soc.*, *133*, 191–213, doi:10.1144/gsjgs.133.3.0191.

Sibson, R. H. (1986), Brecciation processes in fault zones - inferences from earthquake rupturing, *Pure Appl. Geophys.*, *124*, 159–175, doi:10.1007/BF00875724.

Smith, R. B. (1975), Unified theory of the onset of folding, boudinage and mullion structure, *Geol. Soc. Am. Bull.*, *86*, 1801–1809.

Smith, R. B. (1977), Formation of folds, boudinage, and mullions in non-Newtonian materials, *Geol. Soc. Am. Bull.*, *88*, 312–320, doi:10.1130/0016-7606(1977)88<312:FOFBAM>2.0.CO;2.

Stewart, I. S., and P. L. Hancock (1991), Scales of structural heterogeneity within neotectonic normal-fault zones in the Asegean region, *J. Struct. Geol.*, *13*, 191–204, doi:10.1016/0191-8141(91)90066-R.

Wang, W. B., and C. H. Scholz (1994), Wear processes during frictional sliding of rock - a theoretical and experimental-study, *J. Geophys. Res.*, *99*(B4), 6789–6799, doi:10.1029/93JB02875.

Wilson, B., T. Dewers, Z. Reches, and J. Brune (2005), Particle size and energetics of gouge from earthquake rupture zones, *Nature*, *434*, 749–752, doi:10.1038/nature03433.

Wong, H. C., N. Umehara, and K. Kato (1998), The effect of surface roughness on friction of ceramics sliding in water, *Wear*, *218*, 237–243, doi:10.1016/S0043-1648(98)00208-7.

Woodcock, N. H., and K. Mort (2008), Classification of fault breccias and related fault rocks, *Geol. Mag.*, *145*, 435–440.

Zoback, M. D. (1987), New Evidence on the State of Stress on the San Andreas Fault System, *Science*, *238*, 1105–1111, doi:10.1126/science.238.4830.1105.

E. E. Brodsky, Department of Earth and Planetary Sciences, University of California, Santa Cruz, CA 95064, USA. (brodsky@pmc.ucsc.edu)

A. Sagy, Geological Survey of Israel, 30 Malkhe Street, Jerusalem, 95501, Israel. (asagy@gsi.gov.il)